Machine Learning Mapping Approach for Computing Spin Relaxation Dynamics

Mohammad Shakiba, Adam B. Philips, Jochen Autschbach, and Alexey V. Akimov**

Department of Chemistry, University at Buffalo, The State University of New York, Buffalo, NY, 14260 USA.

Abstract: In this work, a machine learning mapping approach for predicting the properties of atomistic systems is reported. Within this approach, the atomic orbital overlap, density, or Kohn-Sham (KS) Fock matrix elements obtained at a low level of theory such as extended tight-binding have been used as input features to predict the electric field gradient (EFG) tensors at a higher level of theory such as those obtained with hybrid functionals. It is shown that the machine-learning-predicted EFG tensors can be used to compute spin relaxation rates of several ions in aqueous solutions. From only a fraction of data used in direct calculation, one can predict the quadrupolar isotropic spin relaxation rates with good accuracy, achieving relative errors between about 1.7-7.6% for different ions.

TOC GRAPHICS

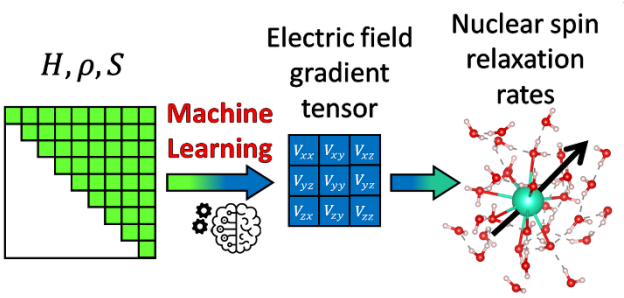

KEYWORDS. Machine learning, electric field gradient, nuclear spin relaxation, kernel ridge regression, atomic guess, extended tight-binding

Nuclear spin relaxation dynamics plays a crucial role in defining nuclear magnetic resonance (NMR) spectra, which provide crucial insight into chemical dynamics at the atomistic scale, with applications, for instance, in biological imaging[1,2] and electrochemical devices.[3,4] Nuclear spin relaxation in diamagnetic species occurs primarily via magnetic dipole-dipole, spin-rotation, and quadrupolar interactions. Quadrupolar nuclides are prevalent in the periodic table, and the quadrupolar relaxation mechanism is known to dominate over the others listed when present.[5]

For a detailed understanding and prediction of quadrupolar nuclear spin relaxation rates, theoretical studies employing molecular dynamics (MD) have become vital. Pioneering studies have relied on force-field (FF) driven MD.[6–13] More recently, it has become possible to conduct NMR relaxation studies based on ab initio molecular dynamics (AIMD) simulations, in which the interatomic forces are calculated via a first-principles electronic structure method usually by using density functional theory (DFT) combined with a classical treatment of the nuclear motion.[14–23] This approach allows for an accurate treatment of sub-picosecond interactions of atoms and molecules which is the driving force of NMR relaxation in the fast motion regime applicable, e.g., for small molecules in solution at not too low temperatures.

For the purpose of calculating nuclear spin relaxation, irrespective of whether they are of the ab-initio or FF type, MD simulations need to be paired with calculations of the relevant interaction tensors that drive a given relaxation mechanism. For instance, quadrupolar relaxation is mediated by the fluctuations of the electric field gradient (EFG) tensor at the nucleus of interest as a function of time. The EFG depends on the distribution of electric charges surrounding the nucleus and therefore has a nuclear and electronic

contribution. The former is usually calculated classically from the distribution of nuclear (point) charges, which is obtained straightforwardly from each point along an MD trajectory. The latter requires the electron density and therefore – in in principle – the electronic EFG needs to be calculated via quantum mechanics (QM) electronic structure methods. For the latter, there are numerous choices of varying accuracy available, without or with periodic boundary conditions. For example, some of us previously benchmarked DFT-based EFG calculations with periodic boundary conditions vs. 'molecular' calculations using cluster models extracted from MD trajectories and showed that both are capable of delivering comparable quadrupolar relaxation rates when the same functionals are employed.[15] In the latter type of calculations, a much larger variety of electronic structure models can be employed.

However, the computational cost of evaluating EFG tensors for hundreds or thousands of MD configurations can quickly become prohibitive. For example, ^{23}Na relaxation, a nuclide that is ubiquitous in humans, has been shown to be useful to investigate cartilage damage in vivo.[24,25] T_2 measurements of $^{23}Na^+$ have also been used in a pioneering study of spinal disk degeneration.[26] MD simulations of such processes likely require large-scale FFMD simulations, which means they need to be accompanied by highly efficient computational methods for EFG tensors. One class of approaches uses structural data from the MD trajectories, atomic partial charges, and models to describe the polarization of the electron density surrounding the nuclide of interest to determine the EFG at essentially the same computational cost of an MD step.[8,27,28] For example, based on partial atomic charges surrounding an ion in solution and the resulting 'external' EFG, Sternheimer antishielding factors[29–33] γ_∞ have been employed to obtain the total EFG at

these ions including the ion polarization from the external EFG by multiplying by a factor $(1+\gamma_\infty)$.[6,8,13,27] The square of this factor enters the relaxation rate. Note that this Sternheimer antishielding is far from being a small correction. For instance, a value of $\gamma_\infty = -5.45$ was reported for Na^+.[34] The Sternheimer model neither accounts for solute polarization due to steric effects, nor for EFGs due to partially covalent solvent-solute interactions such as hydrogen bonds. Therefore, the general utility of the Sternheimer approach has been questioned as being overly reductive.[17,21] Force-fields with ion polarization terms may perform more reliably if properly parameterized,[8] but there is the perennial question of transferability and whether such an approach also works for highly polarizable ions (for example, $\gamma_\infty = -162$ for I^-)[34] or covalently bonded atoms.

As an alternative to the currently available approaches, the present work introduces the use of machine-learning (ML) aided calculations of EFG tensors for the purpose of MD-based quadrupolar nuclear spin relaxation. The immediate advantage of such a method is that it has the potential to provide access to large systems and the dynamics with long correlation times affecting the spin relaxation at a modest computational cost. ML techniques have recently become widely adopted in various scientific domains. For instance, they have been used to accelerate calculations of different properties of molecules,[35–38] solid-state materials,[39,40] and proteins[41,42] where the cost of standard calculations grows rapidly with the size of the system. The acceleration of MD simulations with the help of ML-based interatomic potentials[43–48] enabled modeling systems with millions of atoms. Advanced ML models such as AlphaFold[42] exceled at identifying the binding sites in proteins and predicting their structures. ML techniques have been successfully utilized to perform excited state dynamics simulations in model spin-boson

systems,[49,50] small molecules,[51,52] large graphene nanoribbons with thousands of atoms,[53] light-harvesting complexes,[54] metal nanoclusters,[55] to name a few. ML-based techniques have also been used to extend the length of the dynamical simulation, either by forecasting the longer-time behavior of the observed properties directly using the short-time data[56–61] or by predicting the properties such as state energies and couplings needed for such calculations.[62–64]

Furthermore, ML techniques can be used to elevate the quality of properties extracted from MD studies performed at lower levels of theory. For instance, Shakiba and Akimov[65] recently demonstrated that a simple kernel ridge regression (KRR) method can be used to map a guess Kohn-Sham (KS) Fock operator (based on a superposition of atomic densities) with non-hybrid exchange-correlation functionals, such as Perdew-Burke-Ernzerhof (PBE),[66] to a nearly-converged KS Fock operator computed using more computationally-demanding hybrid functionals such as Heyd-Scuseria-Ernzerhof (HSE06)[67,68] or Becke-Lee-Yang-Parr (B3LYP).[69–72] Instead of directly mapping molecular geometries to molecular properties using complex deep neural networks (NNs), in the aforementioned approach the geometries are first mapped to preprocessed data computed at lower levels of theory. The preprocessed data are then used as input to the ML model and mapped to the properties of interest corresponding to a higher level of theory. Only a few configurations along the precomputed trajectory are needed to generate the reference data at the desired level of theory. Depending on the system size and the length scale of the process to study, the resulting speed-up from the ML assistance can reach several orders of magnitude.[65]

In this work, we extend the ML-based KS Fock operator mapping approach to the calculation of EFG tensors in the context of quadrupolar spin relaxation calculations (Figure 1). Similar to the ML workflow outlined above, we aim to utilize the geometry-sensitive guess atomic orbital overlap, density, or KS Fock matrix elements computed with low-cost electronic structure methods as feature vectors to predict the EFG tensor for nuclear spin-relaxation calculations.

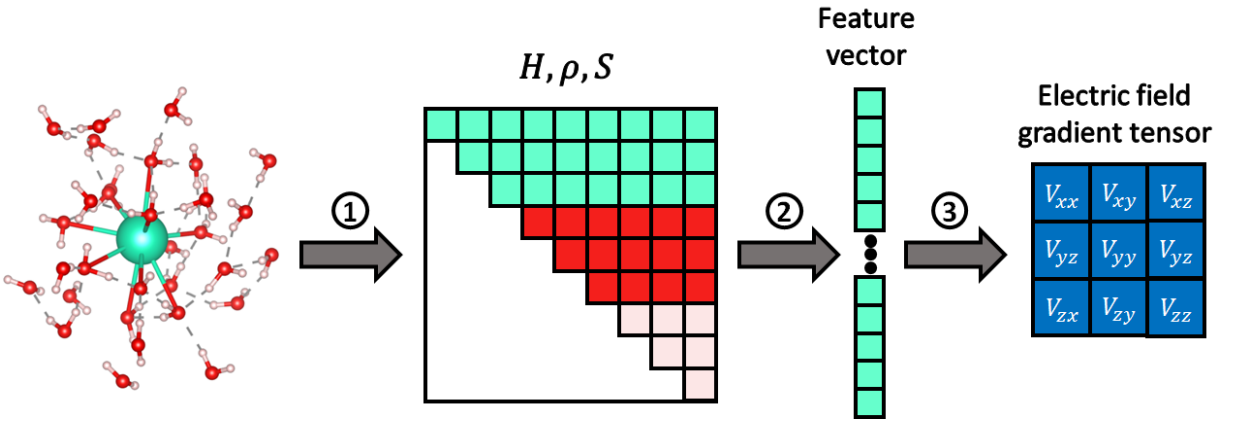

Figure 1. Workflow of the ML mapping approach: (1) the geometry is initially preprocessed by a quantum chemistry software at a low level of theory, such as a tight binding model or an atomic guess with a non-hybrid density functional, and the corresponding atomic overlap, density, and KS Fock matrices are generated; (2) the elements of the matrix corresponding to the interaction of an atom with all other atoms (or its nearest neighbor atoms) are selected as elements of the feature vector; (3) the feature vector is used to predict a set of properties using ML techniques.

NMR relaxation is characterized by the longitudinal (T_1) and transverse (T_2) relaxation times and their inverse, the relaxation rates, respectively. The formalism is based on NMR relaxation theory[73,74] as summarized by Spiess[75], and as implemented by us in the 'dynpy' software[76]. In the limit of fast motion and isotropic samples (solutions, gas phase), R_1 and R_2 are equal and we can

define an isotropic relaxation time (T_{iso}) and rate R_{iso}.[15,17,18] The corresponding spin relaxation rates can be computed as:

$$\frac{1}{T_{\text{iso}}} = \frac{e^2Q^2(2I+3)}{40I^2(2I-1)\hbar^2} G_{\text{iso}}^Q. \quad (1)$$

Here, Q is the spectroscopic nuclear quadrupole moment cross section, e is the unit charge, $\hbar$ is the reduced Planck constant, and I is the nuclear spin quantum number. The function G_{iso}^Q is given by:

$$G_{\text{iso}}^Q = 2\sum_m g_{2,m}(\omega_0). \quad (2)$$

The spectral densities $g_{2,m}(\omega) = \int_0^\infty f_{2,m}(t)\exp(i\omega t)dt$ are the half-Fourier transforms of the EFG tensor autocorrelation functions (ACFs) $f_{2,m}(t) = \langle R_{2,m}(t_0)R_{2,m}^*(t_0+t)\rangle$ written here in terms of EFG spherical tensor elements $R_{\ell,m}$, where $\ell = 2$ indicates the rank of the tensor and $m = -\ell \ldots \ell$ in integer steps. The angle brackets indicate an ensemble average over time origins, t_0. The $R_{2,m}$ are related to the Cartesian EFG tensor components $V_{\alpha\beta}$ ($\alpha, \beta \in \{x, y, z\}$) as:

$$R_{2,0} = 3\sqrt{\frac{1}{6}}V_{zz}, \qquad R_{2,\pm1} = \mp V_{xz} - iV_{yz}, \qquad R_{2,\pm2} = \frac{1}{2}\left(V_{xx} - V_{yy}\right) \pm iV_{xy}. \quad (3)$$

In the fast motion limit, the above Fourier transforms reduce to simple integrations to obtain the spectral densities, $g_{2,m}$, without the frequency dependence. The normalization of the total spectral density gives the correlation time, τ_c as:

$$\tau_c = \frac{1}{\langle V(0)^2\rangle} \quad (4)$$

where $\langle V(0)^2\rangle = \sum_m \langle R_{2,m}(t_0)R_{2,m}^*(t_0)\rangle$. Combining equations (1), (2), and (4) gives the relaxation rate as:

$$\frac{1}{T_{\text{iso}}} = 2C^Q\tau_c\langle V(0)^2\rangle \quad (5)$$

where $C^Q = \frac{e^2Q^2(2I+3)}{40I^2(2I-1)\hbar^2}$ is the prefactor on the right-hand side of equation (1).

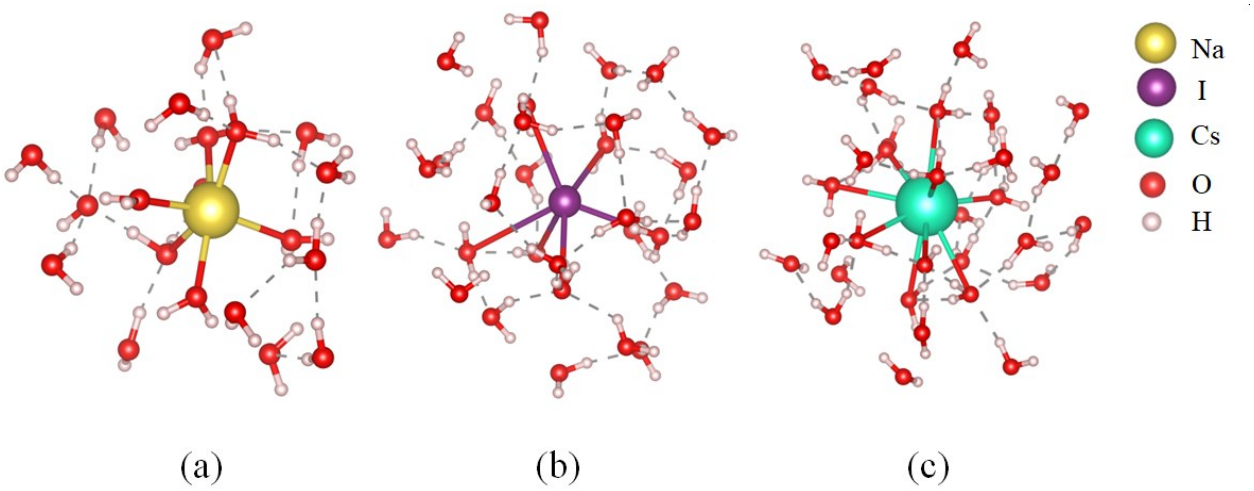

Figure 2. Truncated MD snapshots of solvated (a) sodium, (b) iodine, and (c) cesium ions.

In this work, we consider aqueous sodium, iodine, and cesium ions (Figure 2), for which quadrupolar relaxation rates were previously calculated by some of us.[15,17] The Car-Parinello molecular dynamics (CPMD)[77] trajectories were performed previously and simulated one analyte ion, 64 water molecules, and a counter ion (either a proton or hydroxide) in cubic simulation cells with periodic boundary conditions. The simulations used ultrasoft pseudopotentials[78] from pslibrary 1.0.0,[79] a fictitious electron mass of μ = 450 au, and an integration time step of 0.145 fs. As they were originally performed for independent investigations, the sodium trajectory utilized the PBE exchange-correlation functional[66] and an elevated temperature of 350K to prevent the known 'glass-like' behavior of water in room-temperature simulations of water.[80] The iodide and cesium simulations were equilibrated at 300K and employed the revised revPBE functional.[81,82] Each simulation also included Grimme's D-2 dispersion corrections.[83,84] The production phases of the CPMD simulations were all conducted in the NVE ensemble to a simulation length of 40 ps. Out of 4,000 configurations sampled, 500 snapshots at equal time intervals (ions clustered with 30 nearest neighbor solvent molecules) are used herein to sample the EFG tensor components

computed at the DFT level with PBE0 functional[85] with the ADF software package.[86] These snapshot DFT calculations are the computational bottleneck of the approach. For example, each individual iodide cluster calculation took an average of 40 minutes to converge the SCF and obtain the EFG tensor using ADF. Full computational details for DFT-level computation of the EFGs can likewise be found in references 15 and 17. The ACFs of the EFG tensor components are then used to compute the spin-relaxation times according to equations 1 to 5 using the dynpy software.[76]

The ML model used is a KRR model with either linear and quadratic kernels. The KRR approach has recently been used by Charpentier[87] in a similar context to construct a ML framework with smooth overlap of atomic positions (SOAP)[88] descriptors. Such an approach enabled accurate prediction of NMR tensors, which was leveraged in simulation of NMR spectra and incorporating finite-temperature effects for large-scale sodium silicate glass models at the computational cost of classical MD simulations.

In the KRR approach, the input and output data are scaled to a mean value of zero and a standard deviation of 1.0. The KRR model is obtained through solving the following equations and then is used to predict the EFG matrix elements:

$$v\left[\boldsymbol{V}\left(\boldsymbol{R}(t_i)\right)\right] = \sum_{\alpha=1}^{N_{train}} \boldsymbol{K}\left(v\left[\boldsymbol{X}\left(\boldsymbol{R}(t_i)\right)\right], v[\boldsymbol{X}(\boldsymbol{R}(t_\alpha))]\right)\boldsymbol{c}_\alpha \quad (6)$$

where $\boldsymbol{K}(\boldsymbol{X},\boldsymbol{Y}) = \boldsymbol{X}\boldsymbol{Y}^T$ and $\boldsymbol{K}(\boldsymbol{X},\boldsymbol{Y}) = (\boldsymbol{X}\boldsymbol{Y}^T)^2$ are for linear and quadratic kernels respectively. Here, bold notation is used to indicate vectors and matrices, $v[\boldsymbol{X}]$ notation represents the vectorized form of the corresponding matrix $\boldsymbol{X}$, and $v\left[\boldsymbol{X}\left(\boldsymbol{R}(t_\alpha)\right)\right]$ represents the input feature vector extracted from either atomic orbital overlap, density, or KS Fock matrix. Mathematically, the KRR with linear kernel is essentially the same as the standard linear regression with regularization (ridge regression). However, the use of the KRR framework allows exploring other choices of the kernel

function, such as quadratic kernel which is also used in this work. Finally, the vectors of KRR coefficients are computed for each configuration $\boldsymbol{R}(t_\alpha)$ as:

$$\boldsymbol{c}_\alpha = (\boldsymbol{K} + \lambda \boldsymbol{I})^{-1} v[\boldsymbol{V}(\boldsymbol{R}(t_\alpha))] \quad (7)$$

in which λ is a hyperparameter, selected as 0.1 here, to prevent overfitting. The hyperparameter is tuned with trial and error. As alluded to above, the guess KS Fock matrices in the atomic orbital basis computed with the non-hybrid PBE functional can be used as feature vectors that constitute inputs of the ML model, while the components of the EFG tensors computed at the PBE0/basis level[85] act as the target outputs. In addition to the choice of guess (non-self-consistent, non-SCF) KS Fock matrix, we consider other possibilities for the feature vector choices: (a) guess (non-SCF) density matrices in the AO basis, and (b) atomic orbital overlap matrices. Although none of these choices capture true intrinsic electrostatics of the system, they all are sensitive to the system's geometry. As was shown previously, the structure of an unconverged KS Fock may closely resemble that of a converged (the self-consistent, SCF) one.[65] Since the EFG tensor matrix elements directly depend on the latter, one may expect that the EFG tensor elements can be well-parameterized by the mapping of the non-SCF KS Fock or density matrices. In addition to using non-SCF matrices computed with the PBE functional, we also consider SCF matrices but computed using even more computationally-efficient extended tight-binding (xTB) method.[89] All the feature vector calculations are conducted using the CP2K software.[90,91] To facilitate and accelerate training of the ML models, the matrices are computed using only a limited shell of atoms surrounding the analyte ions. Due to symmetry, only the upper triangular part of these matrices is chosen, vectorized, and used as feature vector to map to the EFG tensors using ML (see section S1 of the Supporting Information).

A few points regarding the present methodology are worth mentioning. First, while alternative geometry-sensitive input features, such as SOAP-based descriptors that are widely used in ML-based force fields,[92] may be used, the present work aims to demonstrate the possibility of the mapping of the geometry-sensitive electronic structure-informed descriptors to the EFG tensor elements. The present method for ML model construction is simple to implement, DFT-informed, and rather efficient. While it is true that SOAP approach does not require even the low-cost DFT or xTB calculations and thus may be computationally inexpensive, the current method represents a conceptually distinct way to generate feature vectors for the EFG tensor elements prediction. Second, the present ML mapping approach is not meant to be globally transferable as ML-based force fields, but rather provides a way to accelerate the calculations of the EFG tensor elements for a given system and under conditions (such as temperature and concentration) used for ML training. Hence, the method is most useful for calculations involving multiple and/or long MD trajectories while the target system/conditions remain unchanged. The approach is expected to be transferable within small variations of temperatures and ion concentrations, as long as no phase transitions occur within such ranges. Third, at the moment, we utilize the simplest approach which does not impose any additional restrictions in regard to rotational covariance of input features such as those used with SOAP-based descriptors. Unlike pretrained ML models,[87] this model is designed to work for a fixed (Cartesian) coordinate system, so the lack of rotational covariance is not critical in this context. It is expected, however, that enforcing the rotational covariance properties in the later versions of the method may help reduce the amount of data needed to reach the desired threshold of accuracy in the target properties and alleviate the overfitting problem.

We explore the quality of the ML mapping approach when the ML is trained using different amounts of the training data: 1%, 2.5%, 5%, 10%, 25%, and 50% of the available data used in

producing the reference quantities. The training samples are constructed by randomly selecting the indicated fraction of the data points (configurations and associated quantum-mechanical data) from the initial dataset without repetitions. Better approaches are likely possible, where the training points would be selected as the most dissimilar points in the available dataset. The data extraction and preparation are done using Libra code,[93,94] and ML procedures are carried out using the scikit-learn package.[95] The mean absolute error between the predicted EFG tensor elements and all reference elements, including both training and test data points, is computed as follows:

$$\epsilon_V = \frac{1}{9}\sum_{\alpha=x,y,z}\sum_{\beta=x,y,z}|V_{ref_{\alpha,\beta}} - V_{ML_{\alpha,\beta}}|, \quad (8)$$

where V_{ref} and V_{ML} represent the reference and ML predicted EFG tensor matrices respectively. We also compute the relative errors in the predicted spin-relaxation times, τ_{iso}, rates, $\frac{1}{T_{\mathrm{iso}}}$, the EFG tensor variances ($\langle V(0)^2\rangle$), and correlation times (τ_c), with respect to their reference values:

$$\epsilon = \frac{|P_{ref} - P_{ML}|}{P_{ref}} \times 100. \quad (9)$$

where P_{ref} and P_{ML} correspond to the reference and ML-predicted properties P, respectively. All additional details of the calculations are available via a Zenodo repository.[96]

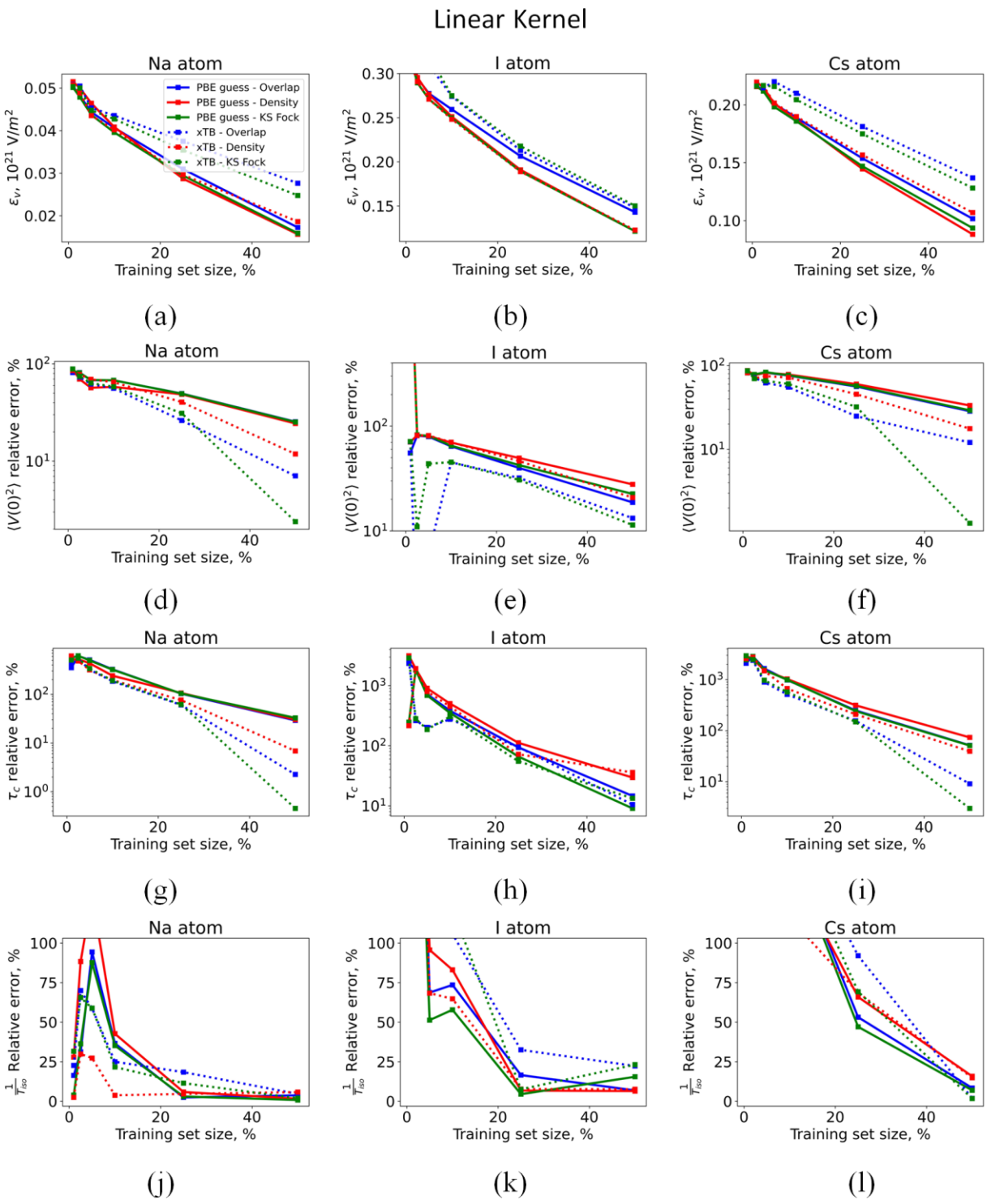

Figure 3. (a, b, c) Mean absolute error of the ML-predicted EFG tensor elements; relative errors of (d, e, f) variance of EFG tensor elements, (g, h, i) correlation times, and (j, k, l)

isotropic relaxation rates. Columns correspond to different ions: (d, g, j) sodium, (e, h, k) iodine, and (f, I, l) cesium. In all panels, the computed properties are computed using atomic orbital overlap (blue), density (red), and KS Fock (green) matrices as the input to ML model. The input are obtained using PBE guess (solid lines) or converged xTB (dashed lines) calculations. All results correspond to ML models trained using a linear kernel.

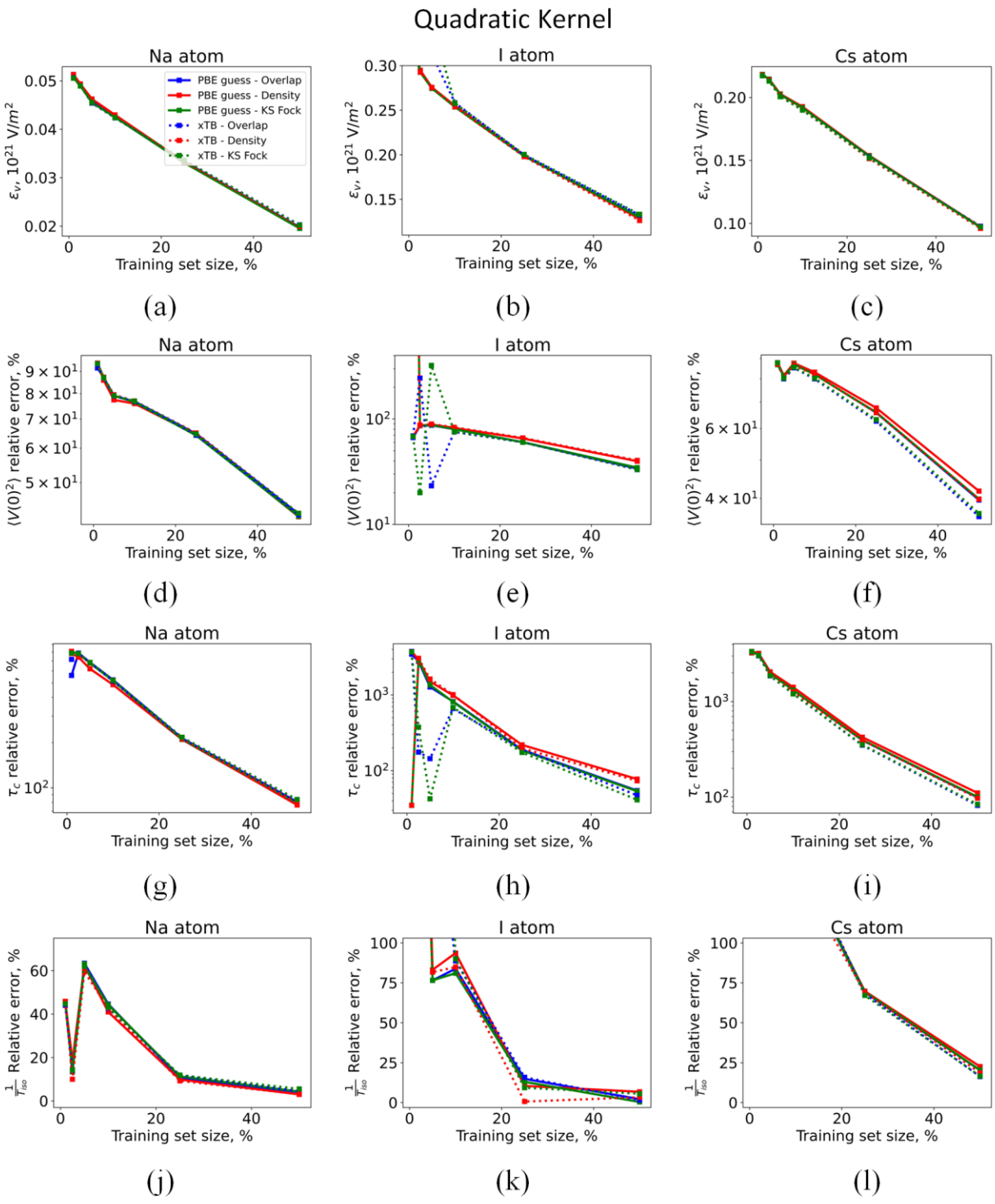

Figure 4. (a, b, c) Mean absolute error of the ML-predicted EFG tensor elements; relative errors of (d, e, f) variance of EFG tensor elements, (g, h, i) correlation times, and (j, k, l) isotropic relaxation rates. Columns correspond to different ions: (d, g, j) sodium, (e, h, k)

iodine, and (f, I, I) cesium. In all panels, the computed properties are computed using atomic orbital overlap (blue), density (red), and KS Fock (green) matrices as the input to ML model. The input are obtained using PBE guess (solid lines) or converged xTB (dashed lines) calculations. All results correspond to ML models trained using quadratic kernel.

The MAEs of the EFG tensor elements computed according to equation 6 are shown in panels a-c of Figures 3 and 4. The MAE consistently decreases as the training set size increases regardless of the atomic type (Na, I, or Cs), input feature type (atomic orbital overlap, density, or KS Fock matrices), kind of calculations (atomic guess or converged xTB), or the choice of kernel (linear or quadratic polynomials). Using the inputs based on the PBE atomic guess leads to better performance with relatively small errors when a linear kernel is employed (Figure 3a-3c). Specifically, using the linear kernel, the use of the density matrix as the ML input leads to smaller errors compared to the use of the KS Fock and overlap matrices. In turn, the choice of the KS Fock matrices is preferred over the atomic orbital overlap matrix since it leads to smaller MAE values, especially as the training set size increases. While the use of the quadratic kernel does not lead to a significant reduction of error (Figure 4, panels a-c), it makes the ML-based predictions relatively insensitive to the kind of the input feature used.

Reproducing the EFG tensor matrix elements is necessary but not sufficient for computing spin relaxation rates accurately. Thus, we also analyze the quality of ML-predicted properties that enter equations 1 to 5. Specifically, we focus on the relative errors in EFG tensor variance, $\langle V(0)^2 \rangle$, and correlation time, τ_c, which are the main components in computing spin relaxation rates. The smallest relative errors in $\langle V(0)^2 \rangle$

and τ_c are obtained when using the largest training set (50% of data), using the converged xTB KS Fock matrix as the feature input, and using a linear kernel in the KRR procedure. For the investigated systems, the relative errors are 2.4% and 0.5% for sodium (Na) ion, 11.4% and 13.3% for iodine (I) ion, and 1.3% and 3.0% for cesium (Cs) ion for $\langle V(0)^2 \rangle$ and τ_c respectively (Figure 3, panels d-i). Despite the fact that the MAE values obtained for ML calculations based on the xTB feature vectors are larger than those calculated using PBE atomic guess matrices (Figure 3, panels a-c), the relative errors are smaller in the former case, for both $\langle V(0)^2 \rangle$ (Figure 3, panels d-f) and τ_c (Figure 3, panels g-i). As a result of such an "error cancellation", the xTB-based spin relaxation rates are comparable in accuracy to those derived from the ML approach based on the PBE-guess feature vectors, sometimes even exceeding them in accuracy. For instance, using the largest training set considered, the relative error of Na spin relaxation rates is 0.8% for the PBE-guess KS Fock, whereas the xTB-based KS Fock input feature yields comparable 1.9% of relative error in rates compared to the reference values obtained from standard calculations. More comprehensively, the relative errors in predicted spin relaxation rates computed using 50% of the data taken at the ML training stage are summarized in Table 1. Furthermore, the reference and predicted individual components of the EFG tensors for each ion trained with different input features using 50% of training data with linear and quadratic kernels are brought in section S2 of the Supporting Information.

Table 1. The spin relaxation rates (in Hz) and the corresponding relative errors (in parenthesis) obtained using ML models trained with 50% of data taken as the training set. The values are reported for atomic orbital overlap, density, and KS Fock matrices taken as the input feature vectors. The results are reported for ML models constructed

with linear and quadratic kernels (separated by the backslash) and using either converged xTB or PBE guess properties. The reference relaxation rates computed directly are shown in the last column.

Ion	Relaxation rate	Guess	Input property, Hz (% relative error)			Reference,[15,17] Hz
			Atomic orbital overlap	Density	KS Fock	
Na	Isotropic	PBE guess	12.41 (3.8)/13.42 (4.1)	12.68 (1.7)/13.28 (3.0)	12.79 (0.8)/13.45 (4.3)	12.89
		xTB	13.50 (1.9)/13.47 (4.4)	12.15 (5.8)/13.29 (3.0)	12.65 (1.9)/13.61 (5.5)	
I	Isotropic	PBE guess	107.00 (6.9)/117.34 (2.1)	107.45 (6.5)/122.66 (6.8)	97.08 (15.5)/115.33 (0.4)	114.88
		xTB	89.26 (22.3)/113.15 (1.5)	123.65 (7.6)/118.72 (3.3)	88.29 (23.2)/108.47 (5.6)	
Cs	Isotropic	PBE guess	67.79 (8.4)/75.24 (20.3)	72.44 (15.8)/76.68 (22.6)	66.91 (7.0)/75.31 (20.4)	62.56
		xTB	63.72 (1.9)/72.77 (16.3)	71.84 (14.8)/74.04 (18.6)	61.48 (1.7)/72.91 (16.5)	

We observe that the present ML mapping approach generally yields lower errors for spin relaxation rates and its components (the variance and correlation time) for Na ion, while for both I and Cs ions larger errors are observed. We rationalize this effect based on the concept of ionic hardness/softness, which is related to the extent of ion's polarizability. The Na ion is less easily polarized, implying that its electronic configuration in solvent is more similar to the isolated ion electronic structure than it is the case for Cs

and I. Cs^+, and in particular I^- are have more easily polarizable electronic shells. Thus, the non-local effects (e.g. due to the presence of solvent molecules) may be more important to account for when computing EFG tensors. Since in the current ML approach, the input matrices are partitioned into smaller blocks of matrix elements, based on the belonging of atomic orbitals to certain atomic species, information on non-local effects may be partially lost. Since in harder ions, such as Na, the non-local effects are less important for determining their properties, the matrix partitioning introduces smaller error in the ML mapping approach, leading to smaller errors in spin relaxation rates compared to Cs and I ions, where non-local effects are more critical to capture.

The current results indicate that the success of the ML models in predicting spin relaxation rates is highly dependent on the complexity of both input features and the selected ML model. Here by “complexity”, we mean both the size of the input vector and the number of nonzero elements which are the interactions between angular momentum components of the atoms in the system. For simpler input features derived from xTB, KRR with a linear kernel performs well, providing accurate predictions for both variance and correlation time. This suggests that the linear kernel is well-suited to capturing the essential relationships in these simpler features. However, when the complexity of the input features increases, such as with the PBE input feature, KRR with neither linear nor quadratic kernel perform as effectively, indicating that more sophisticated ML models, potentially NNs, may be needed to fully exploit the detailed information present in the PBE-guess-based inputs. Conversely, when moving to a quadratic kernel in KRR, we observe a decline in performance especially for xTB features. This outcome implies that while the quadratic kernel is designed to capture more complex nonlinear relations than

the linear kernel, it may lead to overfitting, particularly in the context of the relatively sparse xTB data, which contain larger fraction of zero or near-zero matrix elements compared to the DFT one. This suggests that adding complexity to the kernel does not necessarily provide a better representation of the underlying physics, indicating that simpler input features like the ones generated from xTB are best modeled using simpler kernels. In our initial attempts, not presented in this work, we have explored other kernels. Using higher-degree kernels than the quadratic one and using radial basis function (RBF) kernels yielded results similar to those of the quadratic kernel, without notable improvement. Additional processing of the input features, such as dimensionality reduction by removing features with low variance, may help alleviate the overfitting issue and reduce the error values of the model, although such approaches are outside of the scope of the current proof-of-principle work.

The PBE-guess input features fall into an intermediate category. While they contain more complex information, the KRR models do not fully exploit this potential. The linear kernel cannot properly map these features to the EFG tensors while the quadratic kernel does not offer any significant improvements and, in some cases, worsen the results. This observation highlights an important point: the choice of the input features and the ML model must be aligned. In the current study, the xTB features align well with the capabilities of the KRR with a linear kernel. However, this should not diminish the value of using more complex inputs like the ones generated from PBE-guess. Instead, one should probably explore more advanced ML models, such as NNs, which may be better equipped to handle these inputs and capture the EFG more effectively. Overall, while our current ML approach works well for certain cases, particularly with simpler xTB inputs, it

may not be as effective for other cases. The success of this approach depends on the alignment between the complexity of the input features and the capacity of the ML model to utilize them effectively highlighting the need for careful selection of the model and inputs.

The presented procedure leads to notable speed-ups in EFG tensor elements prediction compared to the reference PBE0 calculations. Once the ML models are constructed, the speed-up is determined by the ratio of the high-level (e.g. PBE0, always self-consistent) and the low-level (self-consistent for xTB or non-self-consistent for PBE). For the systems considered in this work, such ratio is approximately 24-41 and 43-66 times for xTB and PBE atomic guess calculations, respectively (see section S3 of the Supporting Information). Such ratios will be larger for larger systems, due to distinct scaling of computational complexity of the pure and hybrid functionals. Factoring in the costs of the ML model construction, the speed-up is determined by the ratio of the number of MD configurations included in the correlation function calculations to the number of configurations used in the ML model training. In this regard, the main goal/advantage of the method is to accelerate the calculations of the EFG tensors for many geometries (long MD trajectories or multiple distinct MD trajectories) after creating the ML model using a smaller fraction of the MD data.

In conclusion, we develop an ML mapping approach for the prediction of the EFG tensor elements and demonstrate their use for computing quadrupolar nuclear spin relaxation rate. We demonstrate that one can use either the atomic orbital overlap, density, or KS Fock matrices obtained with low levels of electronic structure theory such as converged xTB and or guess PBE as input features. Using either linear or quadratic kernel ridge regression and sufficient amount of training data, such input vectors can be mapped

directly to EFG tensor elements to bypass computationally demanding calculations. Our analysis suggests that all of these feature input options generally yield consistent results. Using the quadratic kernel reduces the variability of the predicted quantities with respect to the choice of the input feature vector types. The developed ML mapping approach yields the results within a few percents of the target values (from the standard calculations) even when a fraction of the input data is used for training the ML model. Better accuracy is obtained for harder, less polarizable ions such as sodium as opposed to more polarizable ones such as cesium or iodide. Overall, our findings validate the efficiency and robustness of the ML mapping approach for predicting the EFG matrices which can significantly reduce the computational costs while yielding good accuracy. The computational acceleration in predicting the time-series of EFG tensor elements offered by the present approach opens new possibilities for conducting more accurate spin-relaxation calculations where many long trajectories need to be involved.

Author Information

Corresponding Author

* Email: alexeyak@buffalo.edu Twitter: @AkimovLab

* Email: jochena@buffalo.edu

Notes

The authors declare no competing financial interests.

Acknowledgement

M.S. and A.V.A. acknowledge financial support of the National Science Foundation (NSF) Grant OAC-NSF-2045204. J.A. acknowledges support from NSF grant CHE-2152633. Support of computations was provided by the Center for Computational Research at the University at Buffalo.[97]

References

(1) Inglese, M.; Madelin, G.; Oesingmann, N.; Babb, J. S.; Wu, W.; Stoeckel, B.; Herbert, J.; Johnson, G. Brain Tissue Sodium Concentration in Multiple Sclerosis: A Sodium Imaging Study at 3 Tesla. *Brain* **2010**, *133*, 847–857.

(2) Ouwerkerk, R.; Bleich, K. B.; Gillen, J. S.; Pomper, M. G.; Bottomley, P. A. Tissue Sodium Concentration in Human Brain Tumors as Measured with ^{23}Na MR Imaging. *Radiology* **2003**, *227*, 529–537.

(3) Pecher, O.; Carretero-González, J.; Griffith, K. J.; Grey, C. P. Materials' Methods: NMR in Battery Research. *Chem. Mater.* **2017**, *29*, 213–242.

(4) Hwang, J.-Y.; Myung, S.-T.; Sun, Y.-K. Sodium-Ion Batteries: Present and Future. *Chem. Soc. Rev.* **2017**, *46*, 3529–3614.

(5) Kowalewski, J.; Mäler, L. Nuclear Spin Relaxation in Liquids: Theory, Experiments, and Applications; Taylor & Francis: New York, **2006**.

(6) Roberts, J. E.; Schnitker, J. Ionic Quadrupolar Relaxation in Aqueous Solution: Dynamics of the Hydration Sphere. *jpc* **1993**, *97*, 5410–5417.

(7) Carof, A.; Salanne, M.; Charpentier, T.; Rotenberg, B. Accurate Quadrupolar NMR Relaxation Rates of Aqueous Cations from Classical Molecular Dynamics. *J. Phys. Chem. B* **2014**, *118*, 13252–13257.

(8) Carof, A.; Salanne, M.; Charpentier, T.; Rotenberg, B. On the Microscopic Fluctuations Driving the NMR Relaxation of Quadrupolar Ions in Water. *J. Chem. Phys.* **2015**, *143*, 194504.

(9) Odelius, M.; Holz, M.; Laaksonen, A. Quadrupolar Relaxation of ^{21}Ne, ^{83}Kr, and ^{131}Xe Dissolved in Acetonitrile. A Molecular Dynamics Study. *J. Phys. Chem. A* **1997**, *101*, 9537–9544.

(10) Odelius, M.; Laaksonen, A.; Levitt, M. H.; Kowalewski, J. Intermolecular Dipole-Dipole Relaxation. A Molecular Dynamics Simulation. *J. Magn. Reson., Ser. A* **1993**, *105*, 289–294.

(11) Odelius, M. Molecular Dynamics Simulations of Quadrupolar Relaxation of \ch^131Xe in Methanol. An Ellipsoidal Picture of the Electric Field Gradient Tensor. *J. Phys. Cehm.* **1994**, *98*, 12108–12116.

(12) Chubak, I.; Alon, L.; Silletta, E. V.; Madelin, G.; Jerschow, A.; Rotenberg, B. Quadrupolar $^{23}Na^{+}$ NMR Relaxation as a Probe of Subpicosecond Collective Dynamics in Aqueous Electrolyte Solutions. *Nat. Commun.* **2023**, *14*, 84.

(13) Chubak, I.; Scalfi, L.; Carof, A.; Rotenberg, B. NMR Relaxation Rates of Quadrupolar Aqueous Ions from Classical Molecular Dynamics Using Force-Field Specific Sternheimer Factors. *J. Chem. Theory Comput.* **2021**, *17*, 6006–6017.
(14) Schmidt, J.; Hutter, J.; Spiess, H.; Sebastiani, D. Beyond Isotropic Tumbling Models: Nuclear Spin Relaxation in Liquids from First Principles. *ChemPhysChem* **2008**, *9*, 2313–2316.
(15) Philips, A.; Marchenko, A.; Truflandier, L. A.; Autschbach, J. Quadrupolar NMR Relaxation from Ab-Initio Molecular Dynamics: Improved Sampling and Cluster Models vs. Periodic Calculations. *J. Chem. Theory Comput.* **2017**, *13*, 4397–4409.
(16) Philips, A.; Marchenko, A.; Ducati, L. C.; Autschbach, J. Quadrupolar ^{14}N NMR Relaxation from Force-Field and Ab-Initio Molecular Dynamics in Different Solvents. *J. Chem. Theory Comput.* **2019**, *15*, 509–519.
(17) Philips, A.; Autschbach, J. Quadrupolar NMR Relaxation of Aqueous $^{127}I^-$, ^{131}Xe, and $^{133}Cs^+$: A First-Principles Approach from Dynamics to Properties. *J. Chem. Theory Comput.* **2020**, *16*, 5835–5844.
(18) Philips, A.; Autschbach, J. Proton NMR Relaxation from Molecular Dynamics: Intramolecular and Intermolecular Contributions in Water and Acetonitrile. *Phys. Chem. Chem. Phys.* **2019**, *21*, 26621–26629.
(19) Philips, A.; Autschbach, J. Unified Description of Proton NMR Relaxation in Water, Acetonitrile, and Methane from Molecular Dynamics Simulations in the Liquid, Supercritical and Gas Phases. *J. Phys. Chem. B* **2023**, *127*, 1167–1177.
(20) Abella, L.; Philips, A.; Autschbach, J. The Sodium Anion Is Strongly Perturbed in the Condensed Phase Even Though It Appears like a Free Ion in NMR Experiments. *J. Phys. Chem. Lett.* **2020**, *11*, 843–850.
(21) Aidas, K.; Ågren, H.; Kongsted, J.; Laaksonen, A.; Mocci, F. A Quantum Mechanics/Molecular Dynamics Study of Electric Field Gradient Fluctuations in the Liquid Phase. The Case of Na+ in Aqueous Solution. *Phys. Chem. Chem. Phys.* **2013**, *15*, 1621–1631.
(22) Komorovsky, S.; Jakubowska, K.; Świder, P.; Repisky, M.; Jaszuński, M. NMR Spin–Spin Coupling Constants Derived from Relativistic Four-Component DFT Theory—Analysis and Visualization. *J. Phys. Chem. A* **2020**, *124*, 5157–5169.
(23) Charpentier, T.; Ispas, S.; Profeta, M.; Mauri, F.; Pickard, C. J. First-Principles Calculation of ^{17}O, ^{29}Si, and ^{23}Na NMR Spectra of Sodium Silicate Crystals and Glasses. *J. Phys. Chem. B* **2004**, *108*, 4147–4161.
(24) Borthakur, A.; Mellon, E.; Niyogi, S.; Witschey, W.; Kneeland, J. B.; Reddy, R. Sodium and $T_{1\rho}$ MRI for Molecular and Diagnostic Imaging of Articular Cartilage. *NMR Biomed.* **2006**, *19*, 781–821.
(25) Madelin, G.; Jerschow, A.; Regatte, R. R. Sodium Relaxation Times in the Knee Joint in Vivo at 7T. *NMR Biomed.* **2012**, *25*, 530–537.
(26) Ooms, K. J.; Cannella, M.; Vega, A. J.; Marcolongo, M.; Polenova, T. The Application of ^{23}Na DQF NMR Spectroscopy for the Study of Spinal Disc Degeneration. *Magn. Reson. Med.* **2008**, *60*, 246–252.
(27) Carof, A.; Salanne, M.; Charpentier, T.; Rotenberg, B. Accurate Quadrupolar NMR Relaxation Rates of Aqueous Cations from Classical Molecular Dynamics. *J. Phys. Chem. B* **2014**, *118*, 13252–13257.

(28) Mocci, F.; Laaksonen, A.; Lyubartsev, A.; Saba, G. Molecular Dynamics Investigation of ^{23}Na NMR Relaxation in Oligomeric DNA Aqueous Solution. *J. Phys. Chem. B* **2004**, *108*, 16295–16302.
(29) Sternheimer, R. On Nuclear Quadrupole Moments. *Phys. Rev.* **1950**, *80*, 102–103.
(30) Sternheimer, R. Nuclear Quadrupole Moments. *Phys. Rev.* **1951**, *84*, 244–253.
(31) Sternheimer, R. M. Shielding and Antishielding Effects for Various Ions and Atomic Systems. *Phys. Rev.* **1966**, *146*, 140–160.
(32) Sternheimer, R. M. Quadrupole Shielding and Antishielding Factors for Several Atomic Ground States. *Phys. Rev. A* **1972**, *6*, 1702–1709.
(33) Sternheimer, R. M. Shielding and Antishielding of Nuclear Quadrupole Moments. *Zeitschrift für Naturforschung A* **1986**, *41A*, 24–36.
(34) Schmidt, P. C.; Sen, K. D.; Das, T. P.; Weiss, A. Effect of Self-Consistency and Crystalline Potential in the Solid State on Nuclear Quadrupole Sternheimer Antishielding Factors in Closed-Shell Ions. *Phys. Rev. B* **1980**, *22*, 4167–4179.
(35) Huang, B.; von Lilienfeld, O. A. Ab Initio Machine Learning in Chemical Compound Space. *Chem. Rev.* **2021**, *121*, 10001–10036.
(36) Duan, C.; Liu, F.; Nandy, A.; Kulik, H. J. Putting Density Functional Theory to the Test in Machine-Learning-Accelerated Materials Discovery. *J. Phys. Chem. Lett.* **2021**, *12*, 4628–4637.
(37) Yamada, H.; Liu, C.; Wu, S.; Koyama, Y.; Ju, S.; Shiomi, J.; Morikawa, J.; Yoshida, R. Predicting Materials Properties with Little Data Using Shotgun Transfer Learning. *ACS Cent. Sci.* **2019**, *5*, 1717–1730.
(38) Kananenka, A. A.; Yao, K.; Corcelli, S. A.; Skinner, J. L. Machine Learning for Vibrational Spectroscopic Maps. *J. Chem. Theory Comput.* **2019**, *15*, 6850–6858.
(39) Westermayr, J.; Marquetand, P. Machine Learning for Electronically Excited States of Molecules. *Chem. Rev.* **2021**, *121*, 9873–9926.
(40) Zhuo, Y.; Mansouri Tehrani, A.; Brgoch, J. Predicting the Band Gaps of Inorganic Solids by Machine Learning. *J. Phys. Chem. Lett.* **2018**, *9*, 1668–1673.
(41) Vamathevan, J.; Clark, D.; Czodrowski, P.; Dunham, I.; Ferran, E.; Lee, G.; Li, B.; Madabhushi, A.; Shah, P.; Spitzer, M.; Zhao, S. Applications of Machine Learning in Drug Discovery and Development. *Nat. Rev. Drug Discov.* **2019**, *18*, 463–477.
(42) Abramson, J.; Adler, J.; Dunger, J.; Evans, R.; Green, T.; Pritzel, A.; Ronneberger, O.; Willmore, L.; Ballard, A. J.; Bambrick, J.; Bodenstein, S. W.; Evans, D. A.; Hung, C.-C.; O'Neill, M.; Reiman, D.; Tunyasuvunakool, K.; Wu, Z.; Žemgulytė, A.; Arvaniti, E.; Beattie, C.; Bertolli, O.; Bridgland, A.; Cherepanov, A.; Congreve, M.; Cowen-Rivers, A. I.; Cowie, A.; Figurnov, M.; Fuchs, F. B.; Gladman, H.; Jain, R.; Khan, Y. A.; Low, C. M. R.; Perlin, K.; Potapenko, A.; Savy, P.; Singh, S.; Stecula, A.; Thillaisundaram, A.; Tong, C.; Yakneen, S.; Zhong, E. D.; Zielinski, M.; Žídek, A.; Bapst, V.; Kohli, P.; Jaderberg, M.; Hassabis, D.; Jumper, J. M. Accurate Structure Prediction of Biomolecular Interactions with AlphaFold 3. *Nature* **2024**, *630*, 493–500.
(43) Keith, J. A.; Vassilev-Galindo, V.; Cheng, B.; Chmiela, S.; Gastegger, M.; Müller, K.-R.; Tkatchenko, A. Combining Machine Learning and Computational Chemistry for Predictive Insights Into Chemical Systems. *Chem. Rev.* **2021**, *121*, 9816–9872.
(44) Butler, K. T.; Davies, D. W.; Cartwright, H.; Isayev, O.; Walsh, A. Machine Learning for Molecular and Materials Science. *Nature* **2018**, *559*, 547–555.

(45) Kulichenko, M.; Barros, K.; Lubbers, N.; Li, Y. W.; Messerly, R.; Tretiak, S.; Smith, J. S.; Nebgen, B. Uncertainty-Driven Dynamics for Active Learning of Interatomic Potentials. *Nat. Comput. Sci.* **2023**, *3*, 230–239.
(46) Fedik, N.; Zubatyuk, R.; Kulichenko, M.; Lubbers, N.; Smith, J. S.; Nebgen, B.; Messerly, R.; Li, Y. W.; Boldyrev, A. I.; Barros, K.; Isayev, O.; Tretiak, S. Extending Machine Learning beyond Interatomic Potentials for Predicting Molecular Properties. *Nat. Rev. Chem.* **2022**, *6*, 653–672.
(47) Fedik, N.; Nebgen, B.; Lubbers, N.; Barros, K.; Kulichenko, M.; Li, Y. W.; Zubatyuk, R.; Messerly, R.; Isayev, O.; Tretiak, S. Synergy of Semiempirical Models and Machine Learning in Computational Chemistry. *J. Chem. Phys.* **2023**, *159*, 110901.
(48) Pinheiro, M.; Ge, F.; Ferré, N.; Dral, P. O.; Barbatti, M. Choosing the Right Molecular Machine Learning Potential. *Chem. Sci.* **2021**, *12*, 14396–14413.
(49) Rodríguez, L. E. H.; Ullah, A.; Espinosa, K. J. R.; Dral, P. O.; Kananenka, A. A. A Comparative Study of Different Machine Learning Methods for Dissipative Quantum Dynamics. *Mach. Learn. Sci. Technol.* **2022**, *3*, 045016.
(50) Ullah, A.; Dral, P. O. Speeding up Quantum Dissipative Dynamics of Open Systems with Kernel Methods. *New J. Phys.* **2021**, *23*, 113019.
(51) Chen, W.-K.; Liu, X.-Y.; Fang, W.-H.; Dral, P. O.; Cui, G. Deep Learning for Nonadiabatic Excited-State Dynamics. *J. Phys. Chem. Lett.* **2018**, *9*, 6702–6708.
(52) Hu, D.; Xie, Y.; Li, X.; Li, L.; Lan, Z. Inclusion of Machine Learning Kernel Ridge Regression Potential Energy Surfaces in On-the-Fly Nonadiabatic Molecular Dynamics Simulation. *J. Phys. Chem. Lett.* **2018**, *9*, 2725–2732.
(53) Wang, Z.; Dong, J.; Qiu, J.; Wang, L. All-Atom Nonadiabatic Dynamics Simulation of Hybrid Graphene Nanoribbons Based on Wannier Analysis and Machine Learning. *ACS Appl. Mater. Interfaces* **2022**, *14*, 22929–22940.
(54) Cignoni, E.; Cupellini, L.; Mennucci, B. Machine Learning Exciton Hamiltonians in Light-Harvesting Complexes. *J. Chem. Theory Comput.* **2023**, *19*, 965–977.
(55) Habib, A.; Lubbers, N.; Tretiak, S.; Nebgen, B. Machine Learning Models Capture Plasmon Dynamics in Ag Nanoparticles. *J. Phys. Chem. A* **2023**, *127*, 3768–3778.
(56) Herrera Rodríguez, L. E.; Kananenka, A. A. Convolutional Neural Networks for Long Time Dissipative Quantum Dynamics. *J. Phys. Chem. Lett.* **2021**, *12*, 2476–2483.
(57) Dral, P. O.; Barbatti, M.; Thiel, W. Nonadiabatic Excited-State Dynamics with Machine Learning. *J. Phys. Chem. Lett.* **2018**, *9*, 5660–5663.
(58) Kawada, R.; Endo, K.; Yuhara, D.; Yasuoka, K. MD-GAN with Multi-Particle Input: The Machine Learning of Long-Time Molecular Behavior from Short-Time MD Data. *Soft Matter* **2022**, *18*, 8446–8455.
(59) Lin, K.; Peng, J.; Gu, F. L.; Lan, Z. Simulation of Open Quantum Dynamics with Bootstrap-Based Long Short-Term Memory Recurrent Neural Network. *J. Phys. Chem. Lett.* **2021**, *12*, 10225–10234.
(60) Lin, K.; Peng, J.; Xu, C.; Gu, F. L.; Lan, Z. Trajectory Propagation of Symmetrical Quasi-Classical Dynamics with Meyer-Miller Mapping Hamiltonian Using Machine Learning. *J. Phys. Chem. Lett.* **2022**, *13*, 11678–11688.
(61) Lin, K.; Peng, J.; Xu, C.; Gu, F. L.; Lan, Z. Automatic Evolution of Machine-Learning-Based Quantum Dynamics with Uncertainty Analysis. *J. Chem. Theory Comput.* **2022**, *18*, 5837–5855.

(62) Akimov, A. V. Extending the Time Scales of Nonadiabatic Molecular Dynamics via Machine Learning in the Time Domain. *J. Phys. Chem. Lett.* **2021**, *12*, 12119–12128.
(63) How, W. B.; Wang, B.; Chu, W.; Tkatchenko, A.; Prezhdo, O. V. Significance of the Chemical Environment of an Element in Nonadiabatic Molecular Dynamics: Feature Selection and Dimensionality Reduction with Machine Learning. *J. Phys. Chem. Lett.* **2021**, *12*, 12026–12032.
(64) Wang, B.; Chu, W.; Prezhdo, O. V. Interpolating Nonadiabatic Molecular Dynamics Hamiltonian with Inverse Fast Fourier Transform. *J. Phys. Chem. Lett.* **2022**, *13*, 331–338.
(65) Shakiba, M.; Akimov, A. V. Machine-Learned Kohn–Sham Hamiltonian Mapping for Nonadiabatic Molecular Dynamics. *J. Chem. Theory Comput.* **2024**, *20*, 2992–3007.
(66) Perdew, J. P.; Burke, K.; Ernzerhof, M. Generalized Gradient Approximation Made Simple. *Phys. Rev. Lett.* **1996**, *77*, 3865–3868.
(67) Heyd, J.; Scuseria, G. E.; Ernzerhof, M. Hybrid Functionals Based on a Screened Coulomb Potential. *J. Chem. Phys.* **2003**, *118*, 8207–8215.
(68) Krukau, A. V.; Vydrov, O. A.; Izmaylov, A. F.; Scuseria, G. E. Influence of the Exchange Screening Parameter on the Performance of Screened Hybrid Functionals. *J. Chem. Phys.* **2006**, *125*, 224106.
(69) Becke, A. D. Density-Functional Exchange-Energy Approximation with Correct Asymptotic Behavior. *Phys. Rev. A* **1988**, *38*, 3098–3100.
(70) Lee, C.; Yang, W.; Parr, R. G. Development of the Colle-Salvetti Correlation-Energy Formula into a Functional of the Electron Density. *Phys. Rev. B* **1988**, *37*, 785–789.
(71) Becke, A. D. Density- functional Thermochemistry. I. The Effect of the Exchange-only Gradient Correction. *J. Chem. Phys.* **1992**, *96*, 2155–2160.
(72) Stephens, P. J.; Devlin, F. J.; Chabalowski, C. F.; Frisch, M. J. Ab Initio Calculation of Vibrational Absorption and Circular Dichroism Spectra Using Density Functional Force Fields. *J. Phys. Chem.* **1994**, *98*, 11623–11627.
(73) Bloembergen, N.; Purcell, E. M.; Pound, R. V. Relaxation Effects in Nuclear Magnetic Resonance Absorption. *Phys. Rev.* **1948**, *73*, 679–715.
(74) Redfield, A. G. On the Theory of Relaxation Processes. *IBM J. Res. Dev.* **1957**, *1*, 19–31.
(75) Spiess, H. W. Rotation of Molecules and Nuclear Spin Relaxation. In *NMR Basic Principles and Progress*; P. Diehl, R. K., E. Fluck, Ed.; Springer: Berlin, **1978**; Vol. 15, pp 55–214.
(76) Philips, A.; Autschbach, J. Dynpy, 2024. https://doi.org/10.5281/zenodo.13241475 (Accessed 14-11-2024).
(77) Car, R.; Parrinello, M. Unified Approach for Molecular Dynamics and Density-Functional Theory. *Phys. Rev. Lett.* **1985**, *55*, 2471–2474.
(78) Kresse, G.; Joubert, D. From Ultrasoft Pseudopotentials to the Projector Augmented-Wave Method. *Phys. Rev. B* **1999**, *59*, 1758.
(79) Dal Corso, A. Pseudopotentials Periodic Table: From H to Pu. *Comput. Mater. Sci.* **2014**, *95*, 337–350. https://doi.org/10.1016/j.commatsci.2014.07.043.

(80) Sit, P. H.-L.; Marzari, N. Static and Dynamical Properties of Heavy Water at Ambient Conditions from First-Principles Molecular Dynamics. *J. Chem. Phys.* **2005**, *122*, 204510.
(81) Zhang, Y.; Yang, W. Comment on “Generalized Gradient Approximation Made Simple.” *Phys. Rev. Lett.* **1998**, *80*, 890.
(82) Perdew, J. P.; Burke, K.; Ernzerhof, M. Reply to Comment on Generalized Gradient Approximation Made Simple. *Phys. Rev. Lett.* **1998**, *80*, 891.
(83) Grimme, S.; Ehrlich, S.; Goerigk, L. Effect of the Damping Function in Dispersion Corrected Density Functional Theory. *J. Comput. Chem.* **2011**, *32*, 1456–1465.
(84) Grimme, S.; Antony, J.; Ehrlich, S.; Krieg, H. A Consistent and Accurate Ab Initio Parametrization of Density Functional Dispersion Correction (DFT-D) for the 94 Elements H-Pu. *J. Chem. Phys.* **2010**, *132*, 154104.
(85) Adamo, C.; Barone, V. Toward Reliable Density Functional Methods without Adjustable Parameters: The PBE0 Model. *J. Chem. Phys.* **1999**, *110*, 6158–6170.
(86) te Velde, G.; Bickelhaupt, F. M.; Baerends, E. J.; Fonseca Guerra, C.; van Gisbergen, S. J. A.; Snijders, J. G.; Ziegler, T. Chemistry with ADF. *J. Comput. Chem.* **2001**, *22*, 931–967.
(87) Charpentier, T. First-Principles NMR of Oxide Glasses Boosted by Machine Learning. *Faraday Discuss.* **2024**.
(88) Bartók, A. P.; Kondor, R.; Csányi, G. On Representing Chemical Environments. *Phys. Rev. B* **2013**, *87*, 184115.
(89) Bannwarth, C.; Ehlert, S.; Grimme, S. GFN2-xTB—An Accurate and Broadly Parametrized Self-Consistent Tight-Binding Quantum Chemical Method with Multipole Electrostatics and Density-Dependent Dispersion Contributions. *J. Chem. Theory Comput.* **2019**, *15*, 1652–1671.
(90) Kühne, T. D.; Iannuzzi, M.; Del Ben, M.; Rybkin, V. V.; Seewald, P.; Stein, F.; Laino, T.; Khaliullin, R. Z.; Schütt, O.; Schiffmann, F.; Golze, D.; Wilhelm, J.; Chulkov, S.; Bani-Hashemian, M. H.; Weber, V.; Borštnik, U.; Taillefumier, M.; Jakobovits, A. S.; Lazzaro, A.; Pabst, H.; Müller, T.; Schade, R.; Guidon, M.; Andermatt, S.; Holmberg, N.; Schenter, G. K.; Hehn, A.; Bussy, A.; Belleflamme, F.; Tabacchi, G.; Glöß, A.; Lass, M.; Bethune, I.; Mundy, C. J.; Plessl, C.; Watkins, M.; VandeVondele, J.; Krack, M.; Hutter, J. CP2K: An Electronic Structure and Molecular Dynamics Software Package - Quickstep: Efficient and Accurate Electronic Structure Calculations. *J. Chem. Phys.* **2020**, *152*, 194103.
(91) Hutter, J.; Iannuzzi, M.; Schiffmann, F.; VandeVondele, J. Cp2k: Atomistic Simulations of Condensed Matter Systems. *Wiley Interdiscip. Rev. Comput. Mol. Sci.* **2014**, *4*, 15–25.
(92) Unke, O. T.; Chmiela, S.; Sauceda, H. E.; Gastegger, M.; Poltavsky, I.; Schütt, K. T.; Tkatchenko, A.; Müller, K.-R. Machine Learning Force Fields. *Chem. Rev.* **2021**, *121*, 10142–10186.
(93) Shakiba, M.; Smith, B.; Li, W.; Dutra, M.; Jain, A.; Sun, X.; Garashchuk, S.; Akimov, A. Libra: A Modular Software Library for Quantum Nonadiabatic Dynamics. *Softw. Impacts* **2022**, *14*, 100445.
(94) Akimov, A. V. Libra: An Open-Source “Methodology Discovery” Library for Quantum and Classical Dynamics Simulations. *J. Comput. Chem.* **2016**, *37*, 1626–1649.

(95) Pedregosa, F.; Varoquaux, G.; Gramfort, A.; Michel, V.; Thirion, B.; Grisel, O.; Blondel, M.; Prettenhofer, P.; Weiss, R.; Dubourg, V.; Vanderplas, J.; Passos, A.; Cournapeau, D. Scikit-Learn: Machine Learning in Python. J. *Mach. Learn. Res.* **2011**, 12, 2825.
(96) Shakiba, M., Philips, A. B., Autschbach, J., & Akimov, A. V. **2024**. AkimovLab/Project_ML_EFG: v1.0.0 (v1.0.0). Zenodo. https://doi.org/10.5281/zenodo.14159688.
(97) http://hdl.handle.net/10477/79221